RSC Advances

PAPER

View Article Online
View Journal | View Issue

Cite this: *RSC Adv.*, 2020, **10**, 5066

Highly enhanced adsorption performance of tetracycline antibiotics on KOH-activated biochar derived from reed plants†

Chuanqi Zhao, *[a] Junguan Ma,[a] Ziyin Li,[bc] Hui Xia,[a] Huan Liu[a] and Yuesuo Yang[a]

Received 6th November 2019
Accepted 17th January 2020

DOI: 10.1039/c9ra09208k

rsc.li/rsc-advances

Organic pollutants in water are an increasingly prominent problem. Given this challenge, this study investigated the high adsorption capacity of reed-based biochar for use as an adsorbent using the potassium hydroxide (KOH) activation method. We investigated the performance and mechanism of reed-based biochar with respect to the adsorption of a significant contaminant of emerging concern, tetracycline (TC). The effects of pH, contact time, temperature, and initial pollution concentration on the adsorption rate were investigated in detail. The experimental results suggest that the internal structure of activated biochar was loose and porous, and the specific surface area (BET) increased by 194.08 times, reaching 965.31 m^2 g^{-1} after KOH activation. The biochar surface was electronegative, due to the ionization of oxygen-containing functional groups, such as hydroxyl (–OH) and carboxyl (–COOH) groups. Solution pH had only a weak influence on TC adsorption; neutral conditions favored adsorption. The adsorption kinetics and isotherms were represented well by the pseudo-second-order and Freundlich models, respectively. The chemical multilayer adsorption may play an important role in TC adsorption, which was a spontaneous endothermic reaction. The adsorption process occurred more easily after KOH activation and the adsorption capacity of biochar improved by more than 20 times. These results indicate that preparing reed-derived biochar using KOH activation is an effective way to reduce pollution and utilize a waste resource.

1 Introduction

In recent years, pharmaceuticals and personal care products (PPCPs), represented most frequently by antibiotics, have gradually entered the water environment and continue to receive widespread attention. Antibiotics are widely used as drugs to treat human and animal diseases, because they selectively inhibit or affect biological functions. Antibiotics in water mainly include tetracyclines, macrolides, sulfonamides, quinolones, and chloramphenicol.[1] These enter the environment from human excreta, sewage discharged from pharmaceutical factories, medical wastewater from hospitals, animal feed and aquaculture, and other sources.[2] When antibiotics enter the human body or livestock, only a small proportion is digested and absorbed. Most of the antibiotics are excreted in the form of feces after biotransformation.[3] Micro-levels of antibiotics in water do not usually cause acute toxicity; however, long-term exposure could lead to chronic toxicity for organisms in the environment.[4] In addition, widely-used antibiotics can induce the generation of antibiotic-resistant genes (ARGs) in microorganisms,[5–7] which can proliferate and widely disseminate in ecosystems, thereby posing a great danger to human health.[8] Experts have demonstrated that the emergence of "super bacteria" or "multi-drug resistant bacteria" may be associated with the environmental contamination of antibiotics and the killing of microbial communities.[6,9]

Tetracyclines (TCs) have become the most widely used antibiotics in human disease control and animal husbandry and aquaculture.[10] As such, they are the most frequently detected antibiotics in the environment, with abundant antibiotic residues detected in drinking water, rivers, and soils. For example, Hamscher *et al.* found that tetracyclines can be detected in liquid excreta and soil fertilized by excreta at concentrations of 4.0 mg kg^{-1} and 198.7 μg kg^{-1}, respectively.[11] Hirsch *et al.* detected 18 kinds of antibiotics in the water discharged from a sewage treatment plant; the tetracycline concentration was 20 ng L^{-1}.[12] Shen *et al.* found that water in the Huangpu River was significantly polluted by many kinds of antibiotics.[13] Among the antibiotics, the tetracycline levels were the highest. Common methods to remove antibiotics from water currently include anaerobic biodegradation,[14] photocatalytic and ozonation degradation,[15,16] electro-degradation[17] and adsorption.[18,19]

[a]Key Lab of Eco-restoration of Regional Contaminated Environment, Ministry of Education, Shenyang University, Shenyang 110044, China. E-mail: zcqbs@aliyun.com; Fax: +86-24-62267101; Tel: +86-24-62269636

[b]Shenyang Academy of Environmental Sciences, Shenyang 110000, PR China

[c]Liaoning Provincial Key Laboratory for Urban Ecology, Shenyang 110000, PR China

† Electronic supplementary information (ESI) available. See DOI: 10.1039/c9ra09208k

Biodegradation can only be used for biodegradable antibiotics. Advanced oxidation treatment often produces toxic intermediates; therefore, they have certain limitations. Adsorption is a commonly used environmental treatment technology, and has the advantages of being inexpensive, simple to operate, have little secondary pollution, and can remove most pollutants in water. As such, the method has universal applicability. The selection of adsorption materials is a key factor in adsorption performance.

Biochar refers to the solid product produced by the pyrolysis of organic matter in an anoxic or incomplete combustion environment.[20] Biochar materials have recently attracted extensive attentions from researchers worldwide because of their simple preparation methods, wide source of raw materials, and excellent adsorption capacity for both organic and inorganic contaminants.[20–23] The adsorption properties of biochar materials are affected by many factors, including different preparation conditions and different sources of raw materials. These factors cause significant differences in biochar characteristics, including specific surface area, pore structure, and surface hydrophobicity, impacting adsorption performances.[24–26]

In general, the biochar adsorption capacity can be improved through activations, which create a mesoporous structure with a high specific surface area.[27–29] The activation methods mainly include physical activation, chemical activation, and integrated process.[20,30,31] The physical activation usually utilizes CO_2 or water vapor as oxidizing agents at a very high temperature (>850 °C) and does not involve any chemicals; while the chemical activation involves the impregnation of chemical reagents, such as $ZnCl_2$, KOH, and H_3PO_4 with biochar followed by activation in an inert atmosphere.[31,32] Compared to the former, the latter is more effective because of its lower consumption of energy and time.[20] In particular, the chemical activation with the KOH has been extensively developed for the synthesis of activated biocarbons.[30,33,34]

There are many reports on biochar preparation; most of these reports focus on materials derived from agricultural crop residues, animal manure and sewage sludge.[28,30,35–37] However, wetland plants are less used to produce biochar and the related research literatures are also quite limited. The wetland plant wastes are widely distributed and rich in resources; the internal structure is loose, porous, with a large specific surface area. The constituents mainly include cellulose, hemicellulose, and lignin, which contain a large number of hydroxyl, carboxyl, carbonyl and other active groups. The basic framework is composed of carbon elements, which are neutral and can be easily chemically modified. Therefore, further developing the use of wetland plant waste as a biomass adsorbent could increase its recycling value, providing a new optimized choice.

For this study, wetland plant wastes were used to prepare an environmentally friendly porous carbon material, which was then applied in the environmental restoration field. The prepared reed-based biochar was used to adsorb tetracycline (TC) antibiotics. The study then evaluated the influence of pH, adsorption time, pollutant concentration and temperature on adsorption performance. The adsorption performance and mechanism by which the biochar adsorbed antibodies was also assessed.

2 Materials and methods

2.1 Preparation of biochar

First, reeds were obtained from a wetland in winter and were then washed, dried and crushed. The reed-based biochar material was prepared through the carbonization and activation of a certain quality of straw powder in a nickel crucible in a tubular furnace. The effects of different carbonization temperatures (450 °C, 650 °C) and different activation modes (carbonization, KOH activation) on the structural characteristics and adsorption properties of biochar were investigated. In this experiment, the mass ratio of KOH to raw material was 3 : 1. The KOH solution (1 g mL^{-1}) was mixed with the raw materials, soaked for 12 h, dried, and placed in a tube furnace in an oxygen-limited environment. The reaction was conducted at a high temperature for 60 min. After cooling, the sample was washed with 10% hydrochloric acid until it reached a neutral pH. It was then dried for use. To maintain oxygen-limiting conditions, nitrogen protection was carried out throughout the preparation process; the nitrogen rate was controlled at 100 mL min^{-1}. The materials obtained from carbonization were labeled as 450-B and 650-B; the number indicated the preparation temperature. Similarly, the biochars obtained from KOH activation were labeled as 450-K and 650-K.

2.2 Characterization of biochar

The surface morphology of the biochar material was observed using scanning electron microscopy (SEM) (S-4800). The samples were placed on the tape and sprayed with gold, then observed and photographed using SEM. The specific surface area and pore characteristics of the material were analyzed using a Specific Surface and Aperture Analyzer (3H-2000 PS2). The liquid nitrogen was subjected to a low temperature adsorption–desorption method for measurement. The treated sample was degassed by heating and vacuuming it for 6 hours. The temperature was then maintained at 77 K for the N_2 adsorption and desorption experiments. The specific surface area was calculated using the BET and Langmuir models, and the mesoporous distribution was calculated using the BJH model. The surface functional groups of the samples were determined using Fourier transform infrared spectroscopy (FTIR) analysis (IR-960). The KBr tableting method was used with a scanning step size of 1 cm^{-1} and a scanning wavelength range of 400–4000 cm^{-1}. The zeta potential trend of the biochar was measured using a Malvern laser particle size analyzer (Malvern, Nano ZS UK) before and after activation.

2.3 Biochar adsorption performance

Static adsorption experiments were used to test the adsorption properties of biochar. In the adsorption experiments using carbonized biochar (450-B and 650-B), the initial TC concentration in the solution was set between 10 to 50 mg L^{-1}. For the KOH activated biochar, the initial TC concentration in the

solution was set between 60 to 300 mg L^{-1}. The antibiotic solutions were adjusted to different initial pH values (3.0–9.0) using HCl and NaOH; the background solution was 0.02 mol L^{-1} NaCl. A sample of 15 mg adsorbent was added into the brown reaction bottle, mixed evenly, and placed in a constant temperature water bath oscillator (15–40 °C). Different sampling times between 5 min and 24 h were established. In this experiment, the solutions with SO_4^{2-}, CO_3^{2-}, and PO_4^{3-} (0.2 mol L^{-1}) were prepared as the common ions to investigate the effects of ion on adsorption process. The supernatant was filtered through a 0.45 μm membrane and then the equilibrium concentration was determined using an ultraviolet spectrophotometer (U-3900, Hitachi). Three parallel samples were set for each sample and their average values were used for the analysis.

The amount of pollutant on the adsorbent was calculated by the following formula:

$$Q_e = \frac{(C_0 - C_e) \times V}{m} \quad (1)$$

In this expression, Q_e (mg g^{-1}) is the equilibrium adsorption amount of the adsorbent; C_0 and C_e (mg L^{-1}) are the pollutant concentrations at the initial time and the equilibrium time, respectively; V (L) is the volume of the solution; and m (g) is the mass of the adsorbent.

In this experiment, two kinetic models of pseudo-first-order kinetics and pseudo-second-order kinetics were used to simulate the adsorption process of antibiotics onto biochar. The pseudo-first-order kinetic model can be expressed as follows:[28]

$$Q_t = Q_e(1 - e^{-k_1 t}) \quad (2)$$

where Q_e and Q_t (mg g^{-1}) represent the adsorption capacities at the equilibrium time and time t (min), respectively; k_1 (min^{-1}) denotes the pseudo-first-order kinetic adsorption rate constant. Further, the pseudo-second-order kinetic model can be expressed as follows:

$$Q_t = \frac{k_2 Q_e^2 t}{1 + k_2 Q_e t} \quad (3)$$

where k_2 (g mg^{-1} min^{-1}) denotes the pseudo-second-order kinetic rate constant.

The least square method was used for fitting of the above equations and for calculating the initial adsorption rate, v_0, as follows:

$$v_0 = k_2 Q_e^2 \quad (4)$$

At a constant temperature, the relationship between adsorption capacity and equilibrium concentration of solute is called the adsorption isotherm. Commonly used adsorption isotherms include the Langmuir model (eqn (5)) and the Freundlich model (eqn (6)):[19]

$$\frac{C_e}{Q_e} = \frac{C_e}{Q_m} + \frac{1}{Q_m b} \quad (5)$$

$$Q_e = K_f C_e^{1/n} \quad (6)$$

where Q_m denotes the maximum adsorption quantity on the adsorbent surface, (mg g^{-1}); b indicates the constant related to the adsorption energy, (L mg^{-1}); K_f and n denote Freundlich constants related to the adsorption capacity and adsorption intensity, respectively.

The Langmuir model assumes there is no interaction force between adsorbed molecules on the uniform adsorbent surface under isothermal conditions, forming an ideal model independent of adsorption capacity or coverage. The Freundlich model assumes that under isothermal conditions, adsorption occurs on a non-uniform adsorbent surface and active sites with different energies.

The R_L value usually reflects the degree of isothermal adsorption: difficult to adsorb ($R_L > 1$); linear adsorption ($R_L = 1$); easy to adsorb ($0 < R_L < 1$); irreversible adsorption ($R_L = 0$).[35]

$$R_L = \frac{1}{1 + b \times C_0} \quad (7)$$

In the expressions, C_0 is the initial concentration of adsorbate (mg L^{-1}) and b is Langmuir isothermal constant.

The parameters involved in adsorption thermodynamics generally include the enthalpy change (ΔH), entropy change (ΔS), Gibbs free energy (ΔG), and the solid–liquid partition coefficient (K_d). The variable ΔH reflects the heat of the reaction process. The $\Delta H < 0$ indicates that the adsorption reaction is exothermic; when $\Delta H > 0$, the adsorption reaction is endothermic. The variable ΔS indicates the disorderly change of the reaction system. For closed systems, if $\Delta S = 0$, the reaction process is reversible. If $\Delta S > 0$, the reaction is predisposed to proceed spontaneously. The positive and negative values of ΔG signal the possibility of an adsorption reaction. If $\Delta G < 0$, the reaction proceeds spontaneously. In contrast, when $\Delta G > 0$, the reverse reaction proceeds spontaneously.

The following equations were used to calculate the parameters:[38]

$$\Delta G = -RT \ln K_d \quad (8)$$

$$\Delta G = \Delta H - T\Delta S \quad (9)$$

$$\ln K_d = \frac{\Delta S}{R} - \frac{\Delta H}{RT} \quad (10)$$

In these expressions: K_d is the solid–liquid partition coefficient at equilibrium; ΔS is the reaction entropy change in J mol^{-1} K^{-1}; ΔH is the reaction enthalpy change in kJ mol^{-1}; R is the gas constant at 8.314 J mol^{-1} K^{-1}; T is the absolute temperature in K; and ΔG is the free energy of the adsorption reaction in kJ mol^{-1}.

3 Results and discussion

3.1 Biochar characteristics

3.1.1 Surface topography. Microstructure observation was an effective way to reveal the surface characteristics of carbon materials. Fig. 1 showed the SEM image of the reed-based biochar materials. It was found that the unactivated biochar had a smooth, dense surface structure, with no observable

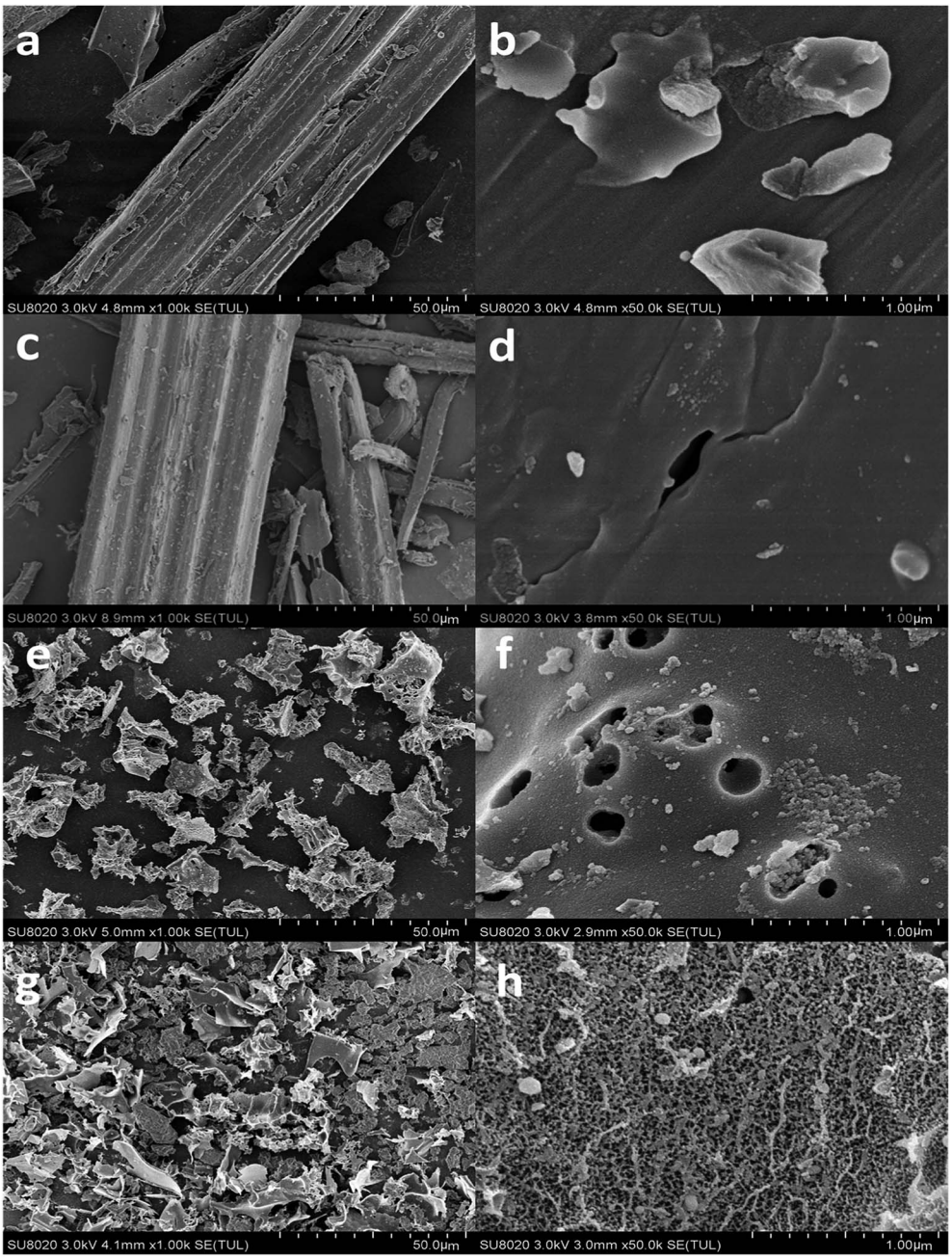

Fig. 1 SEM pictures of reed-based biochar: (a and b) 450-B, (c and d) 650-B, (e and f) 450-K, and (g and h) 650-K.

microporous structure. This indicated that the simple carbonization process created a limited number of pores and did not change the structural characteristics of the reed straw. Adding the activator KOH transformed the original smooth surface of the biochar material into a rough and uneven pleated surface. A large number of microporous structures were produced, as shown in Fig. 1f and h. Comparing the biochar before and after activation showed that the size of the biochar gradually changed from long fibre to fine granular, especially on the 650-K surface, as the original fibre structure could not be seen.

In the present study, KOH was used as activating agent to generate porous structures of the reed-based biochar, the mainly activation mechanism for the KOH activation was as follows:[30,39]

$$4KOH + C = K_2CO_3 + K_2O + 2H_2 \quad (11)$$

$$K_2CO_3 + 2C = 2K + 3CO \quad (12)$$

$$K_2O + 2C = 2K + CO \quad (13)$$

During the activation process, adding KOH first dehydrated the cellulose, hemicellulose, and lignin; K^+ ions then fully entered the interior of the material to generate the pore network. Deep openings were then realized through the etching

of C atoms (eqn (11) and (12)). After that, the as-prepared K_2CO_3 could be efficiently intercalated into the lattices of biaochar during the carbonization at high temperature, which further improved the porous structure of the reed-based samples (see eqn (13)).[30] Salt and excess KOH were removed by washing the sample with distilled water, and a developed pore formed in the etched position. The SEM indicated that although the activator KOH (melting point: 360 °C) melted and started to etch the carbon wall of biochar at 450 °C, the activation effect was limited. When the temperature was raised to 650 °C, the activation reaction became sufficient, resulting in many microporous structures, achieving a high activation effect, and increasing the corresponding loss rate of carbon.

3.1.2 Pore structure. In order to gain insight into the specific surface areas and porous structures of the samples, the N_2 adsorption–desorption analysis was carried out, and the isotherms and pore size distribution curves were shown in Fig. S1.† It was found that the absorption/desorption curves of KOH activated samples exhibited gradually increasing adsorption quantity and spindly hysteresis loops at P/P_0 = 0.0–1.0, which belonged to the characteristics of IV-type isotherms with H3 hysteresis loops. As increasing the activation temperature, the curve of 650-K appeared a narrower desorption hysteresis loop, which suggested that the material had a great deal of small mesoporous structures. The corresponding pore size distribution clearly indicated that the 450-B had a wide pore size distribution, while the samples after KOH activation exhibited a narrow pore size distribution (Fig. S1b, f and h†).

Table 1 described the pore structure of the biochar material. The carbonized biochar material (450-B) had a low specific surface area of only 4.16 $m^2\ g^{-1}$ (BET specific surface area) and 5.94 $m^2\ g^{-1}$ (Langmuir specific surface area) with large pore diameters, reaching 48.34 nm. The pore volume and pore area were relatively low. After adding the activator, both the specific surface area and the pore volume of biochar materials increased significantly, and the average pore size decreased to approximately 3 nm. In contrast, the specific surface area of 450-K increased significantly by 111.59 times to 468.39 $m^2\ g^{-1}$ (BET specific surface area). The pore volume and area also increased by 70.88 times and 194.08 times, respectively. After increasing the temperature to 650 °C, the specific surface area of 650-K further increased to 965.31 $m^2\ g^{-1}$ (BET specific surface area), which was 24.48 times the area of the unmodified carbon material (650-B). The pore volume and pore area also increased by 14 times and 29.44 times, respectively. These results indicated strong activation performance. The rich mesoporous structure would effectively enhance the adsorption capacity of biochar materials.

3.1.3 Surface chemical properties. The surface functional groups of reed-based biochar were characterized using FTIR, which reflected biomass dehydration and pyrolysis. Fig. 2a showed the FTIR spectra of reed biochar prepared using the carbonization and activation methods. Vibration peaks associated with the C=O group appeared at 1630 cm^{-1} and 1403 cm^{-1}. The characteristic peaks at 1580 cm^{-1} were closely related to the C=C of a benzene ring structure.[40] Wide peaks were observed at 1050 cm^{-1}, which were associated with the stretching vibration peak of C–O–C.[41] When comparing the FTIR spectra before and after KOH activation, the –OH peak at 1690 cm^{-1} was weakened, and the C=O group at 1403 cm^{-1} gradually disappeared. In contrast, the absorption peak of C–O–C group was enhanced, indicating that KOH activation caused the dehydration and decarboxylation of reed biochar, improving its aromatization.

Fig. 2b showed the zeta potential of biochar. In the range of the measured pH, the zeta potential was negatively correlated with the pH value. This was due to the ionization of carboxyl and hydroxyl groups on the biochar surface, with the decrease in H^+. When the solution pH was higher than 2, the zeta potential of biochar was negative, and the biochar surface was negatively charged. The zeta potential of biochar changed little after activation, indicating that KOH activation had a weak effect on the electrical properties of the biochar surface.

3.2 Adsorption performance of reed biochar

3.2.1 The impact of pH. Fig. 3 showed the effect of pH on the adsorption process. Changes in the solution pH had a slight influence on the adsorption process. As the pH increased, the adsorption of TC firstly increased and then decreased. The optimal pH at which the four kinds of biochar adsorbed TC was approximately 6.0; the adsorption capacities of the 450-B and 650-B were 6.29 mg g^{-1} and 7.75 mg g^{-1}, respectively. After KOH activation, the adsorption capacities of 450-K and 650-K significantly increased to 49.04 mg g^{-1} and 108.81 mg g^{-1}, representing increases of 6.80 times and 13.04 times, respectively. This indicated strong activation performance. Meanwhile, the results showed that an increase in the activation temperature had little effect on the adsorption performance of the carbonized biochar, but significantly impacted KOH activation.

The form of the antibiotics in solution was related to the change in pH. There were three ionization equilibrium constants of TC in an aqueous solution: pK_{a1} = 3.30, pK_{a2} =

Table 1 Pore structure characteristics of reed-based biochar

Material	BET specific surface area ($m^2\ g^{-1}$)	Langmuir specific surface area ($m^2\ g^{-1}$)	Average pore diameter (nm)	Total pore volume ($cm^3\ g^{-1}$)	Total pore surface area ($m^2\ g^{-1}$)
450-B	4.16	5.94	48.34	0.0032	0.065
650-B	39.43	56.63	8.52	0.03	0.57
450-K	468.39	685.75	3.59	0.23	12.68
650-K	965.31	1412.22	3.48	0.45	17.35

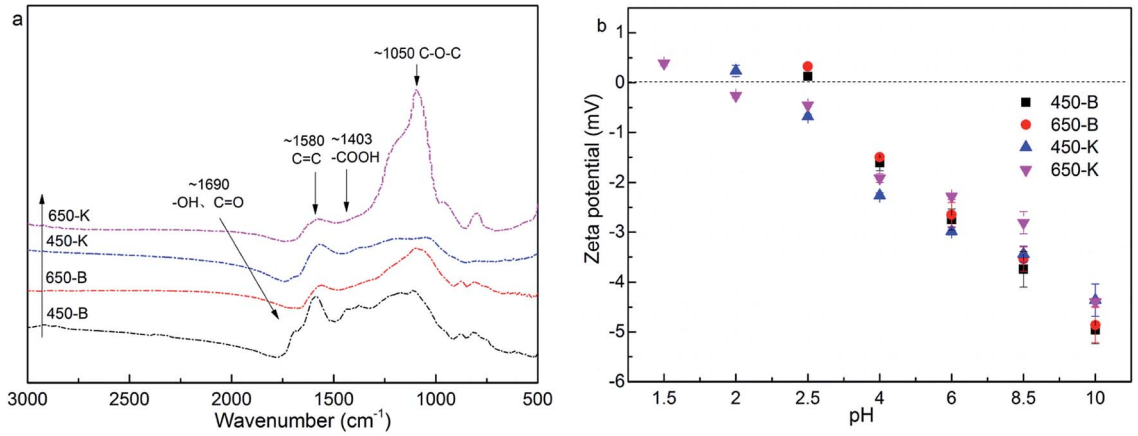

Fig. 2 Surface characters of reed-based biochar: (a) FT-IR pictures, and (b) zeta potential.

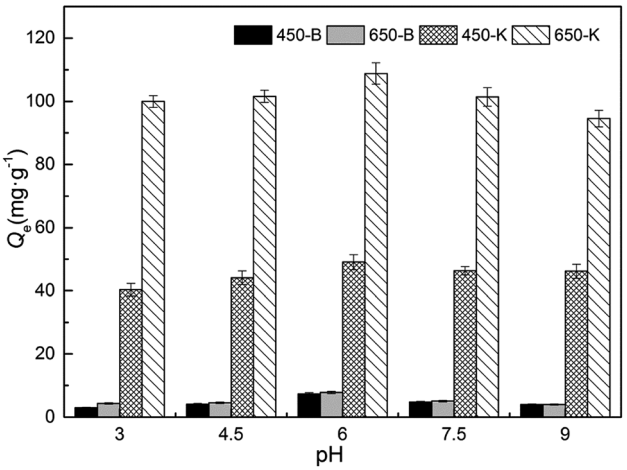

Fig. 3 TC adsorption capacity of four materials at different pH values.

7.68, $pK_{a3} = 9.68$. Therefore, under different pH conditions, it dissociated into four different forms: cationic form (TC^{+}), zwitterionic form ($TC^{\pm}$), anionic form (TC^{-}), and dianion form (TC^{2-}).[42] In this experiment, TC lost its electrons at low pH and was present in the form of TC^{+}. The adsorption performance gradually increased with pH, due to the enhanced interaction between the negatively charged biochar and the positively charged TC. Furthermore, the aromatic ring structure of TC and the sp_2 structure of biochar formed π–π bonds, increasing the adsorption of both. As the pH approached a neutral value, the TC^{+} gradually transformed into the form of amphoteric ions ($TC^{\pm}$). Therefore, interactions such as hydrogen bonding and π–π stacking of biochar surface and TC molecule were enhanced, and biochar showed the highest adsorption capacity under these conditions. As the solution pH became alkaline, the TC was present in the form of a negative charge, such as TC^{-} or TC^{2-}. This produced electrostatic repulsion with the negatively charged biochar, causing adsorption performance to be at its lowest.

3.2.2 Effect of common anions. Common anions in water, including SO_4^{2-}, CO_3^{2-}, and PO_4^{3-}, might compete to be adsorbed on the material surface, which would influence the adsorption performance of biochar. The results of the investigated anions were shown in Table 2. It was found that the adsorption capacity of biochar was affected obviously with the existence of common ions. Specifically, impacts of CO_3^{2-} and PO_4^{3-} on TC adsorption were similar with Q_e decrement by approximately 20%, while SO_4^{2-} greatly influenced the adsorption process with reductions reaching 40%. This behavior could be attributed to the existence of anions that weakened the electrostatic attraction between the adsorbent and TC, thus decreasing the adsorption capacity of biochar.

3.2.3 Effect of adsorption time and kinetics. Fig. 4 showed the effect of adsorption time on the adsorption of TC on biochar materials. The adsorption capacity first increased rapidly, with more than 90% of the TC adsorption completed at this stage. After this, the adsorption rate decreased, gradually reaching equilibrium. At the beginning of adsorption, the abundant pores and functional groups on biochar surface provided sufficient adsorption sites, so pollutant molecules/ions easily attached to the biochar surface. As adsorption occurred, the availability of effective adsorption sites gradually decreased, slowing the adsorption rate until adsorption equilibrium was reached. Meanwhile, the difference in TC concentration in the solid–liquid phase was reduced with the adsorption process, weakening the displacement of residual TC from the solution to the interface of the biochar materials. This slowed the adsorption rate.

To evaluate the speed control step and adsorption mechanism, the pseudo-first-order kinetic model and the pseudo-second-order kinetic model were used to fit the adsorption data. Table 3 showed the fitting results. The adsorption of TC by inactive biochar material was more consistent with the pseudo-first-order kinetic equation. After KOH activation, adsorption became more consistent with the pseudo-second-order kinetics process, with a higher correlation coefficient (R^2). This indicated that KOH activation changed the biochar adsorption mechanism. These results showed that physical diffusion was very important for the adsorption of TC by the original biochar. After activation, the chemical reaction became a speed-

Table 2 Effect of common anions on the adsorption capacities

Materials	0 mol L^{-1} ion strength	Common ions (mol L^{-1})		
		SO_4^{2-}	CO_3^{2-}	PO_4^{3-}
450-B	5.55 ± 0.33	1.28 ± 0.35	3.04 ± 0.42	2.66 ± 0.41
650-B	7.35 ± 0.40	3.89 ± 0.27	5.38 ± 0.31	5.29 ± 0.32
450-K	35.27 ± 1.76	22.37 ± 1.48	26.28 ± 1.59	27.62 ± 1.57
650-K	97.71 ± 2.81	61.71 ± 1.32	76.09 ± 1.52	73.34 ± 2.48

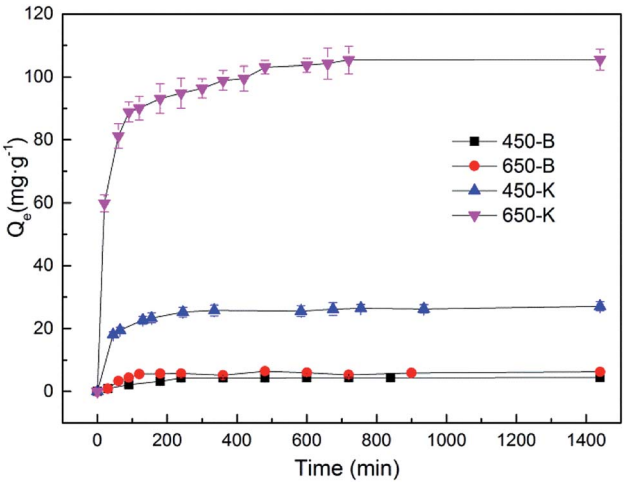

Fig. 4 Effect of adsorption time on the adsorption capacities.

controlling step.[3] Through calculation, it was found that the equilibrium adsorption capacities (Q_e) of TC by 450-B and 650-B were 4.43 and 5.93 mg g^{-1}, respectively. After the activation of KOH, Q_e (adsorption by 450-K and 650-K) increased by 5.14 times and 16.65 times, reaching 27.23 and 104.67 mg g^{-1}, respectively. A comparison of the initial adsorption rate (v_0) of TC by biochars suggested that the adsorption onto activated adsorbent was faster than that of control adsorbent. Compared with the pore information data in Table 1, the specific surface area, pore volume, and area of the reed-based biochar improved after KOH activation, effectively enhancing the adsorption capacity.

3.2.4 Influence of initial concentration and isothermal adsorption equation. Fig. 5 showed the effects of different initial concentrations and temperatures on TC adsorption by biochar. With an increase in the initial concentration, the amount of TC adsorbed by biochar gradually increased. When the initial concentration reached a certain level, the adsorption increment gradually decreased and the adsorption reached equilibrium. In this experiment, two isothermal adsorption models, Langmuir and Freundlich, were selected to fit the equilibrium adsorption. Table 4 showed that the Freundlich isothermal adsorption model had a higher correlation coefficient R^2 before and after biochar activation. This indicated that the Freundlich isothermal adsorption model was a better fit than the Langmuir isothermal adsorption model for the adsorption data of this experiment. The TC adsorption on the surface of carbon materials was consistent with multi-layer heterogeneous adsorption.[43]

The theoretical maximum adsorption capacity (Q_m) was calculated using the Langmuir model. The model showed that the Q_m of biochar greatly improved after KOH activation. In particular, the value for 650-K could be increased by more than 20 times, consistent with the experimental trend. Furthermore, Q_m experienced an increasing trend as the adsorption temperature increased. This indicated that a higher temperature facilitated the adsorption of TC by biochar. R_L was the equilibrium parameter based on the Langmuir model.[35] The R_L of all adsorption processes were between 0 and 1, indicating that TC was easily adsorbed on the reed biochar surface. After KOH activation, the R_L of biochar decreased significantly, indicating that activation made adsorption easier. The value of n calculated from Freundlich model was related to the intensity of the adsorption reaction.[44] The smaller the value of $1/n$, the easier the adsorption was. The data in Table 4 showed that the $1/n$ values of the 450-K and 650-K adsorption processes were significantly lower than the unactivated biochar. This indicated that the biochar had a stronger affinity and adsorption capacity for TC after KOH activation, consistent with the results of R_L.

Table 5 reported the comparison of Q_m values and surface area of the studied adsorbents applied for TC removal. It was found that the reed-based biochar prepared in this work showed obvious advantages both in adsorption capacity and the

Table 3 Parameters of kinetic models of reed-based biochar adsorbing antibiotics

Material	Pseudo-first order			Pseudo-second-order			
	Q_e (mg g^{-1})	$k_1 \times 10^{-2}$ (min^{-1})	R^2	Q_e (mg g^{-1})	$k_2 \times 10^{-4}$ (g mg^{-1} min^{-1})	R^2	v_0 (mg g^{-1} min^{-1})
450-B	4.43	0.83	0.9882	5.01	21.70	0.9644	0.05
650-B	5.93	1.39	0.9333	6.54	28.81	0.8922	0.12
450-K	25.77	2.28	0.9805	27.23	15.31	0.9979	1.14
650-K	98.91	3.70	0.9558	104.67	5.77	0.9934	6.32

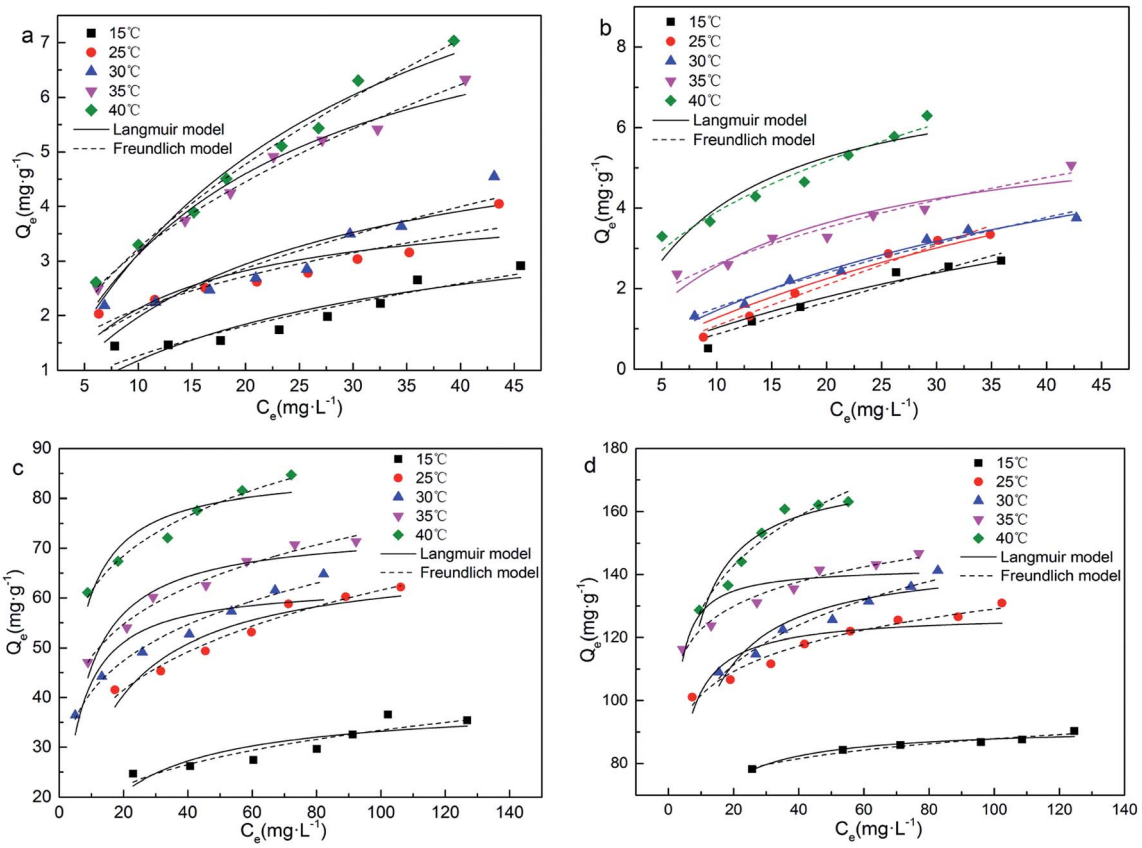

Fig. 5 Effect of initial concentrations and temperatures on the adsorption capacities: (a) 450-B, (b) 650-B, (c) 450-K and (d) 650-K.

specific surface area when compared to others biochars. However, the Q_m was lower than the values reported for graphene and graphene oxide materials. For example, Zhao *et al.* obtained Q_m value of 1805 mg g^{-1} by using TiO_2–graphene sponge as adsorbent for TC removal.[45] Graphene adsorbents had the advantages of high specific surface area and rich

Table 4 Parameters of the Langmuir and Freundlich isothermic models

Material	Temperature (°C)	Langmuir model				Freundlich model		
		Q_m (mg g^{-1})	b (L mg^{-1})	R_L	R^2	K_f (mg g^{-1})	$1/n$	R^2
450-B	15	4.24	0.0385	0.34–0.72	0.8093	0.39	0.5163	0.9050
	25	4.21	0.1021	0.16–0.49	0.7473	0.93	0.3604	0.8925
	30	5.82	0.0511	0.28–0.66	0.7729	0.69	0.4781	0.8956
	35	8.75	0.0554	0.27–0.64	0.9746	1.04	0.4858	0.9904
	40	11.30	0.0383	0.34–0.72	0.9569	0.88	0.5638	0.9864
650-B	15	7.26	0.0164	0.55–0.86	0.9300	0.10	0.9416	0.9379
	25	9.49	0.0155	0.56–0.87	0.9513	0.12	0.9557	0.9682
	30	7.74	0.0232	0.46–0.81	0.9816	0.34	0.6529	0.9741
	35	6.30	0.0682	0.23–0.59	0.8667	0.96	0.4346	0.9502
	40	7.70	0.1079	0.16–0.48	0.8541	1.54	0.4050	0.9466
450-K	15	38.87	0.0585	0.08–0.22	0.7855	10.44	0.2526	0.9154
	25	68.12	0.0734	0.06–0.18	0.8747	19.96	0.2446	0.9630
	30	62.98	0.2150	0.02–0.07	0.8222	25.64	0.2051	0.9811
	35	74.01	0.1654	0.03–0.09	0.8994	31.46	0.1847	0.9784
	40	85.82	0.2415	0.02–0.06	0.8489	42.50	0.1593	0.9768
650-K	15	91.82	0.2183	0.02–0.07	0.9346	60.28	0.0818	0.9539
	25	127.49	0.4147	0.01–0.04	0.7882	80.14	0.1035	0.9639
	30	145.62	0.1653	0.02–0.09	0.8616	70.32	0.1536	0.9644
	35	142.50	0.8697	0.01–0.02	0.7615	101.10	0.0837	0.9657
	40	173.61	0.2626	0.01–0.06	0.8798	91.10	0.1502	0.9328

Table 5 Comparison of Q_m obtained in literature for removal of TC

Adsorbents	Q_m (mg g^{-1})	S_{BET} (m^2 g^{-1})	Reference
Reed-based biochar	173.61	965.31	Present work
Rice straw biochar	21.69	14.185	37
Fe/Zn-biochar	102.0	—	46
Clay–biochar composites	77.962	8.72	47
Graphene oxide	314	—	3
rGOs	219.10	384.5	48
NaOH-activated carbon	455.8	1524	49
Multi-walled carbon nanotubes	192.7	207	50
TiO_2–graphene sponge	1805	—	45

surface active sites, but they also had the common disadvantages of nano-materials such as easy loss and difficult recovery. Although the obtained Q_m of reed-based biochar was lower than values reported for nano-materials, the features such as low cost, excellent stability, high porosity and easy separation, showed other advantages and could overpass this drawback

3.2.5 Thermodynamic analysis. A thermodynamic analysis of TC adsorption by biochar was conducted at different temperatures. Table 6 and Fig. S2† showed the results. At different temperatures, the enthalpy changes of all adsorption processes were positive ($\Delta H > 0$), indicating that the adsorption of TC by biochar was an endothermic reaction. The rise in temperature benefited the adsorption process, which was consistent with the conclusions from the isothermal model analysis. The adsorption entropy change ΔS was positive in Table 6, indicating that the adsorption process was irreversible and the reaction proceeded in the direction of increasing system chaos. The fact that the biochar had a $\Delta G < 0$ indicated that the adsorption process was spontaneous, and the absolute value of ΔG increased gradually with the increase in temperature. This indicated that the rise in temperature facilitated the reaction, which was consistent with the conclusion drawn by the fact that $\Delta H > 0$. The molecular thermal motion, energy transfer, and material transfer on the interface layer between adsorbate and adsorbent slowed down at a low temperature, which was not conducive to the mass transfer of TC. As the system temperature increased, the probability and frequency of contact between the TC and the carbon material surface in the solution significantly increased, improving adsorption efficiency.

Table 6 Thermodynamic experimental parameters of the materials

Material	Temperature (°C)	ΔG (kJ mol^{-1})	ΔS (J mol^{-1} K^{-1})	ΔH (kJ mol^{-1})
450-B	15	−1.02	20.37	4.85
	25	−1.22		
	30	−1.33		
	35	−1.43		
	40	−1.53		
650-B	15	−2.22	30.66	5.61
	25	−2.52		
	30	−2.68		
	35	−2.83		
	40	−2.98		
450-K	15	−2.45	86.01	22.32
	25	−3.31		
	30	−3.74		
	35	−4.17		
	40	−4.60		
650-K	15	−5.01	74.87	16.55
	25	−5.76		
	30	−6.14		
	35	−6.51		
	40	−6.88		

4 Conclusion

The reed-based biochar adsorbent in this study was fabricated using KOH activation and was then used to treat tetracycline-contaminated wastewater through adsorption. The experimental results demonstrated that the internal structure of activated biochar was loose and porous. The specific surface area (650-K) reached 965.31 m^2 g^{-1}, with an average pore size of approximately 3 nm. As such, a neutral pH facilitated the adsorption process. The TC adsorption mechanism of biochar was mainly attributed to π–π conjugation, van der Waals forces, and electrostatic interaction. The TC adsorption by KOH activated biochar conformed to pseudo-second order model and was controlled by chemical reactions. The isotherm data fitted well with the Freundlich model, indicating a multilayer adsorption. The maximum theoretical adsorption capacity (Q_m) of 650-K reached 173.61 mg g^{-1}, increasing by more than 20 times. The thermodynamic analysis showed $\Delta H > 0$, $\Delta S > 0$, and $\Delta G < 0$, suggesting that adsorption of TC by the reed-based biochar was a spontaneous endothermic process, with a temperature increase favoring adsorption. Overall, the reed-based biochar investigated in this research highlights an attractive adsorbent candidate to treat antibiotic-contaminated water, and warrant further study as engineering materials for wastewater treatment.

Conflicts of interest

There are no conflicts of interest to declare.

Acknowledgements

The authors would like to express appreciation to the anonymous reviewers and editors for their valuable comments and suggestions. The authors would like to acknowledge the National Natural Science Foundation of China (41703120), Major Science and Technology Program for Water Pollution Control and Treatment (2018ZX07601-002) and the National Natural Science Foundation of Liaoning Province (2019-ZD-0560).

References

1 F. Yu, Y. Li, S. Han and J. Ma, *Chemosphere*, 2016, **153**, 365–385.
2 J.-L. Liu and M.-H. Wong, *Environ. Int.*, 2013, **59**, 208–224.
3 Y. Gao, Y. Li, L. Zhang, H. Huang, J. Hu, S. M. Shah and X. Su, *Journal of Colloid & Interface Science*, 2012, **368**, 540–546.
4 Y. Liang, M. Pei, D. Wang, S. Cao, X. Xiao and B. Sun, *J. Colloid Interface Sci.*, 2017, **51**, 4988–4998.
5 Y. G. Zhu, T. A. Johnson, J. Q. Su, M. Qiao, G. X. Guo, R. D. Stedtfeld, S. A. Hashsham and J. M. Tiedje, *Proc. Natl. Acad. Sci. U. S. A.*, 2013, **110**, 3435–3440.
6 P. Grenni, V. Ancona and A. Barra Caracciolo, *Microchem. J.*, 2018, **136**, 25–39.
7 Z. Qian-Qian, Y. Guang-Guo, P. Chang-Gui, L. You-Sheng and Z. Jian-Liang, *Environ. Sci. Technol.*, 2015, **49**, 6772–6782.
8 H. W. Hu, J. T. Wang, J. Li, J. J. Li, Y. B. Ma, D. Chen and J. Z. He, *Environ. Microbiol.*, 2016, **18**, 3896–3909.
9 A. Pinheiro, R. M. Rosa Albano, T. C. Alves, V. Kaufmann and M. R. da Silva, *Agric. Water Manag.*, 2013, **129**, 1–8.
10 D.-A. Jia, D.-M. Zhou, Y.-J. Wang, H.-W. Zhu and J.-L. Chen, *Geoderma*, 2008, **146**, 224–230.
11 H. Gerd, S. Silke, H. P. Heinrich and N. Heinz, *Anal. Chem.*, 2002, **74**, 1509.
12 R. Hirsch, T. Ternes, K. Haberer and K.-L. Kratz, *Sci. Total Environ.*, 1999, **225**, 109–118.
13 Q. Shen, X. Ji, S. Fu, Y. Liu and L. Li, *Ecol. Environ.*, 2012, **21**, 1717–1723.
14 A. S. Stasinakis, *Bioresour. Technol.*, 2012, **121**, 432–440.
15 B. Gao, S. Dong, J. Liu, L. Liu, Q. Feng, N. Tan, T. Liu, L. Bo and L. Wang, *Chem. Eng. J.*, 2016, **304**, 826–840.
16 L. Prieto-Rodríguez, I. Oller, N. Klamerth, A. Agüera, E. M. Rodríguez and S. Malato, *Water Res.*, 2013, **47**, 1521.
17 C. I. Brinzila, M. J. Pacheco, L. Ciríaco, R. C. Ciobanu and A. Lopes, *Chem. Eng. J.*, 2012, **209**, 54–61.
18 D. Huang, X. Wang, C. Zhang, G. Zeng, Z. Peng, J. Zhou, M. Cheng, R. Wang, Z. Hu and X. Qin, *Chemosphere*, 2017, **186**, 414.
19 F. Reguyal and A. K. Sarmah, *Sci. Total Environ.*, 2018, **628–629**, 722–730.
20 Q. Huang, S. Song, Z. Chen, B. Hu, J. Chen and X. Wang, *Biochar*, 2019, **1**, 45–73.
21 C. Peiris, S. R. Gunatilake, T. E. Mlsna, D. Mohan and M. Vithanage, *Bioresour. Technol.*, 2017, **246**, 150.
22 J. Heo, Y. Yoon, G. Lee, Y. Kim, J. Han and C. M. Park, *Bioresour. Technol.*, 2019, **281**, 179–187.
23 C. Zhang, G. Zeng, D. Huang, C. Lai, M. Chen, M. Cheng, W. Tang, L. Tang, H. Dong, B. Huang, X. Tan and R. Wang, *Chem. Eng. J.*, 2019, **373**, 902–922.
24 O. Ioannidou and A. Zabaniotou, *Renewable Sustainable Energy Rev.*, 2007, **11**, 1966–2005.
25 X. Kong, Y. Liu, J. Pi, W. Li, Q. J. Liao and J. Shang, *Environ. Sci. Pollut. Res.*, 2017, **24**, 6679–6687.
26 A. N. Ngigi, Y. S. Ok and S. Thiele-Bruhn, *J. Hazard. Mater.*, 2019, **364**, 663–670.
27 A. M. Dehkhoda, E. Gyenge and N. Ellis, *Biomass Bioenergy*, 2016, **87**, 107–121.
28 T. Chen, L. Luo, S. Deng, G. Shi, S. Zhang, Y. Zhang, O. Deng, L. Wang, J. Zhang and L. Wei, *Bioresour. Technol.*, 2018, **267**, 431–437.
29 J. Qin, F. Qin, C. Sun and Q. Yang, *Environ. Prot. Sci.*, 2019, **45**, 25–28.
30 Y. Fu, Y. Shen, Z. Zhang, X. Ge and M. Chen, *Sci. Total Environ.*, 2018, **646**, 1567–1577.
31 A. U. Rajapaksha, S. S. Chen, D. C. W. Tsang, M. Zhang, M. Vithanage, S. Mandal, B. Gao, N. S. Bolan and Y. S. Ok, *Chemosphere*, 2016, **148**, 276–291.
32 M. J. Prauchner, K. Sapag and F. Rodríguez-Reinoso, *Carbon*, 2016, **110**, 138–147.
33 K. Yang, L. Zhu, J. Yang and D. Lin, *Sci. Total Environ.*, 2018, **618**, 1677–1684.
34 R. Acosta, V. Fierro, A. Martinez de Yuso, D. Nabarlatz and A. Celzard, *Chemosphere*, 2016, **149**, 168–176.
35 Z. Junyu, S. Zefeng and Y. Yuesuo, *Water Sci. Technol.*, 2019, **79**, 676–687.
36 D. Wei, B. Li, H. Huang, L. Luo, J. Zhang, Y. Yang, J. Guo, L. Tang, G. Zeng and Y. Zhou, *Chemosphere*, 2018, **197**, 165–180.
37 W. Hua, C. Fang, Q. Wang, Y. Chu, Y. Song, Y. Chen and X. Xue, *RSC Adv.*, 2018, **8**, 16260–16268.
38 Y. Li, C. Zhao, Y. Wen, Y. Wang and Y. Yang, *Environ. Sci. Pollut. Res.*, 2018, **25**, 21036–21048.
39 Z. Li, B. Li, Z. Liu, D. Li, H. Wang and Q. Li, *Electrochim. Acta*, 2016, **190**, 378–387.
40 C. Peng, Y. Zhai, Z. Yun, B. Xu, T. Wang, C. Li and G. Zeng, *Fuel*, 2016, **176**, 110–118.
41 C. H. Chia, B. Gong, S. D. Joseph, C. E. Marjo, P. Munroe and A. M. Rich, *Vib. Spectrosc.*, 2012, **62**, 248–257.
42 C. Zhao, P. Hong, Y. Li, X. Song, Y. Wang and Y. Yang, *J. Chem. Technol. Biotechnol.*, 2019, **94**, 1176–1186.
43 H. Jin, M. U. Hanif, S. Capareda, Z. Chang, H. Huang and Y. Ai, *J. Environ. Chem. Eng.*, 2016, **4**, 365–372.
44 Y. Feng, H. Zhou, G. Liu, J. Qiao, J. Wang, H. Lu, L. Yang and Y. Wu, *Bioresour. Technol.*, 2012, **125**, 138–144.
45 L. Zhao, F. Xue, B. Yu, J. Xie, X. Zhang, R. Wu, R. Wang, Z. Hu, S.-T. Yang and J. Luo, *J. Nanopart. Res.*, 2015, **17**, 16.
46 Y. Zhou, X. Liu, Y. Xiang, P. Wang, J. Zhang, F. Zhang, J. Wei, L. Luo, M. Lei and L. Tang, *Bioresour. Technol.*, 2017, **245**, 266–273.
47 K. S. D. Premarathna, A. U. Rajapaksha, N. Adassoriya, B. Sarkar, N. M. S. Sirimuthu, A. Cooray, Y. S. Ok and M. Vithanage, *J. Environ. Manage.*, 2019, **238**, 315–322.

48 W. Song, T. Yang, X. Wang, Y. Sun, Y. Ai, G. Sheng, T. Hayat and X. Wang, *Environ. Sci.: Nano*, 2016, **3**, 1318–1326.
49 A. C. Martins, O. Pezoti, A. L. Cazetta, K. C. Bedin, D. A. S. Yamazaki, G. F. G. Bandoch, T. Asefa, J. V. Visentainer and V. C. Almeida, *Chem. Eng. J.*, 2015, **260**, 291–299.
50 S. Álvarez-Torrellas, A. Rodríguez, G. Ovejero and J. García, *Chem. Eng. J.*, 2016, **283**, 936–947.